# Supporting Information: Efficient and Stable Wide Bandgap Perovskite Solar Cells through Surface Passivation with Long Alkyl Chain Organic Cations

*The Duong,*[1,*] *, Huyen Pham,*[2] *Yanting Yin,*[3,4] *Jun Peng,*[1] *Md Arafat Mahmud,*[1,**] *YiLiang Wu,*[1] *Heping Shen,*[1] *Jianghui Zheng,*[5,6] *Thanh Tran-Phu,*[7] *Teng Lu,*[8] *Li Li,*[9] *Anand Kumar,*[3,4] *Gunther G. Andersson,*[3,4] *Anita Ho-Baillie,*[5,6] *Yun Liu,*[8] *Thomas White,*[1] *Klaus Weber,*[1] *Kylie Catchpole*[1,*]

[1]School of Engineering, The Australian National University, Canberra 2601, Australia

[2]Department of Electronic Materials Engineering, Research School of Physics, The Australian National University, Canberra 2601, Australia

[3]Flinders Institute for Nanoscale Science and Technology, Flinders University, Adelaide, SA 5042, Australia

[4]Flinders Microscopy and Microanalysis, College of Science and Engineering, Flinders University, Adelaide, SA 5042, Australia

[5]The University of Sydney Nano Institute (Sydney Nano) and School of Physics, University of Sydney, Sydney 2006, Australia

[6]Australian Centre for Advanced Photovoltaics (ACAP), School of Photovoltaic and Renewable Energy Engineering, University of New South Wales, Sydney 2052, Australia

[7]Nanotechnology Research Laboratory, School of Engineering, The Australian National University, Canberra 2601, Australia

[8]Research School of Chemistry, The Australian National University, Canberra 2601, Australia

[9]Australian National Fabrication Facility (ANFF), Department of Electronic Materials Engineering, The Australian National University, Canberra 2601, Australia

*Corresponding Authors: the.duong@anu.edu.au, kylie.catchpole@anu.edu.au

**Present address: The University of Sydney Nano Institute (Sydney Nano) and School of Physics, University of Sydney, Sydney 2006, Australia

## Experimental Procedures

### Materials

Formamidinium iodide, formamidinium bromide, methylammonium iodide, methylammonium bromide, n-butylammonium bromide, n-octylammonium bromide, n-dodecylammonium bromide, TiO2 paste were ordered from GreatCell Solar Materials. Spiro-MeOTAD was ordered from Lum-Tech. Other materials were ordered from Sigma Aldrich.

### Device Fabrication

ITO glass substrates were cut into 1.4 cm * 1.25 cm and were sequentially cleaned in ultrasonic bath with detergent, acetone, and ethanol. Before processing, the substrates were cleaned in UV Ozone for 30 minutes. A compact $TiO_2$ layer (70 nm) was deposited on the substrates by spinning a solution of titanium(IV) isopropoxide (TTIP) in 2-propanol at 5000 rpm for 15 s, followed by an annealing step at 500 $^oC$ for 30 minutes. A layer of mesoporous $TiO_2$ (100 nm) was deposited on the substrates by spinning a solution of $TiO_2$ paste (30NRD) in ethanol at 5000 rpm for 15 s, followed by another annealing step at 500 $^oC$ for 30 minutes. 3D perovskite precursor (1 ml) was prepared by mixing of $FAPbI_2Br$ (750 µl, 1.3 mol in N,N-Dimethylformamide (DMF) / Dimethyl sulfoxide (DMSO) 4:1 volume ratio), $MAPbI_2Br$ (150 µl, 1.3 mol in DMF/DMSO 4:1 volume ratio), $CsPbI_2Br$ (100 µl, 1.3 mol in DMSO) and RbI (50 µl, 1.3 mol in DMSO). Perovskite was deposited on the substrates by spinning the solution (40 µl) at 1000 rpm for 10 s (acceleration rate 100 rpm/s) and 4000 rpm (acceleration rate 1000 rpm/s) for 25 s. Chlorobenzene (150 µl) was quickly dropped on the

middle of the substrates 7 s before the program ends. The film was then annealed at 100°C on a hotplate for 30 minutes. Solution of n-BABr (1.15 mg/ml), n-OABr (2.7 mg/ml) and n-DABr (3.1 mg/ml) in 2-propanol was deposited on the perovskite film at 5000 rpm for 30 s. It is worth noting that the concentrations used in here had been optimized separately for each organic cation material to achieve the best overall performance in each case. The substrate was further annealed at 100°C for 5 minutes. A Spiro-MeOTAD layer (~120 nm) was deposited on the perovskite films by spinning solution of Spiro-MeOTAD (40 µl, 72 mg/ml) in chlorobenzene with Li-TFSI (17.5 µl, 520 mg/ml in acetonitrile) and 4-tBp (28.5 µl) at 4000 rpm for 30 s. An Au contact layer (100 nm) was deposited on the substrates by thermal evaporation through a shadow mask with an active area of 0.16 $cm^2$.

**Characterizations**

The JV characteristic of the opaque perovskite cells was measured using solar simulator model #WAVELABS SINUS-220 equipped with a potentiostat source AutolabPGSTAT302N. The light intensity was calibrated at one Sun (100 $mW/cm^2$, AM1.5G) using the certified FraunhoferCalLab reference cell. The spectra mismatch was calculated to be 0.69%. Unless stated otherwise, the scan rate was fixed at 50 mV/s with a voltage step of 10 mV and dwell time of 200 ms when measuring perovskite solar cells. No device pre-conditioning was applied prior to the JV tests. The devices were kept inside a $N_2$ environment and the temperature was kept at 25 °C during the test. The External Quantum Efficiency (EQE) measurement was carried out using with QXE7 spectral response tool from PV Measurements Inc., with monochromatic light from a xenon arc lamp. The EQE response was calibrated using two calibrated silicon and Ge diodes for 300-1000 nm and 1000-1400 nm wavelength regions, respectively. GIXRD was measured with a high-resolution PANalytical X'Pert PRO MRD system with the step size of 0.005° and the integration time of 1s per step. Reflection/Transmission was measured with a Lambda 1050 spectrophotometer

(Perkin Elmer) in integrating sphere mode. SEM surface and cross-sectional images were taken using a FEI Verios system. The surface morphology mapping was conducted by the Cypher atomic force microscopy (AFM) (Oxford Instrument, Asylum Research, CA, USA). The Ti/Pt-coated tip (AC240TM-R3, Olympus) with calibrated spring constant, $k$= 2.07 N/m (resonace frequency ~ 70 kHz in the air) was adopted to conduct the non-contact imaging. The resultant surface roughness (RMS) is calculated as the Root Mean Square of a 5 × 5 μm surface region. TEM analyses were performed using a JEOL 2100F instrument on perovskite films spun on the carbon side of the copper TEM grid. Steady state photoluminescence measurements and time-resolved photoluminescence measurements were performed using LabRAM HR Evolution system with a time-correlated single photon counting (TCSPC) system (DeltaPro-DD, Horiba). A 508 nm diode laser (DD-510L, Horiba) with pulse duration of 110ps and fluence of ~10 μJ/cm$^2$/pulse, and a repetition rate of 312.5kHz was used for excitation. Photoluminescence images of perovskite solar cells were taken following the procedure reported in our previous work.[1, 2] XPS was conducted in an ultra-high vacuum apparatus from SPECS, which maintains a base pressure at low $10^{-10}$ mbar. The Mg Kα line (12 kV, 200 W) is used for the measurements [3, 4] with an UHV non-monochromatic X-ray source. The angle between the X-ray source and the analyser is 54°. Survey scan at a pass energy of 40 eV was processed first. High-resolution scans at a pass energy of 10 eV were then recorded for Mo, O and C. UPS was applied to determine the occupied electron states of a sample surface [5, 6] and the minimum energy required for an electron to escape the surface (secondary electron). In the measurement, electrons were emitted with a UV radiation of 21.218 eV excitation energy, and thus collected by detector. The UPS was operated with in-situ XPS to avoid any contamination during sample transfer. IPES was used in this work for determining the unoccupied electron states of a sample, [7, 8] which was based on electron in/photon out mechanism. In the experiment, a beam of electron with specified energy was

directed onto a sample surface, entering the unoccupied states and releasing photon with corresponding energy. The photon was detected by ionizing gas phase of a mixed Ar/acetone inside a Geiger-Müller tube. As a function of the kinetic energy of the electrons, the emitted photons allowed comprising the IPES spectrum. By operating in-situ IPES after UPS, a complete energy band structure of the sample was acquired. For determining the WF, the secondary electron cut-off on the binding energy scale of the UPS spectra was analyzed. The WF was taken by calculating the difference between the excitation energy of UV-light, which was 21.22 eV used for UPS, and the peak cut-off along the base line of the spectra. The value of valence band was determined by approximating the base line and the onset of valence electron peak of UPS with a linear curve and determining their intersections.[9] The same procedure was applied for determining the value of conductive band upon the conduction electron peak of IPES. When quantifying the peaks of XPS spectra, the intensity of peaks of various elements were normalized with atomic sensitive factor (ASF).[10] NICISS is a technique to obtain the element depth profile with a resolution of Å of depth of the sample surface. In the NICISS setup, a sample is bombarded with few keV of the pulsed inert gas ion beam (usually $He^+$) which backscatters from the atoms present in the sample. During the backscattering process, ion's projectile experiences energy losses which are converted into concentration depth profile. These energy losses are determined from the time of flight (TOF) of the projectile after hitting the sample and backscattering to the detector.[11] The elemental profile is determined using the stopping power of He ions previously calculated by Alharbi *et al.*.[12]

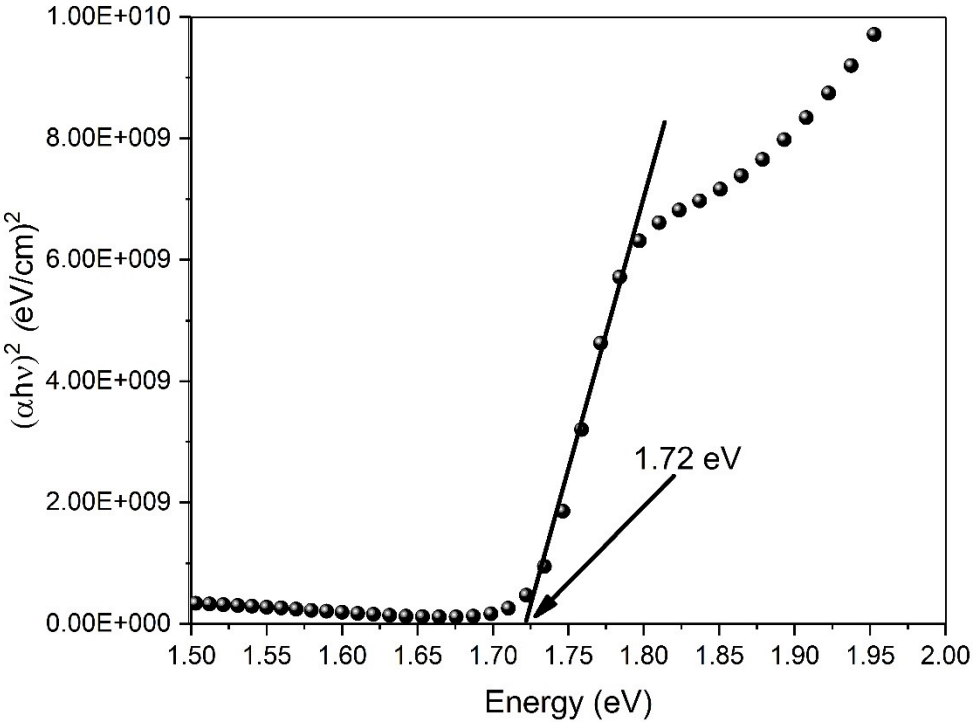


**Figure S1.** Tauc plot showing the bandgap of the perovskite composition used in this work.

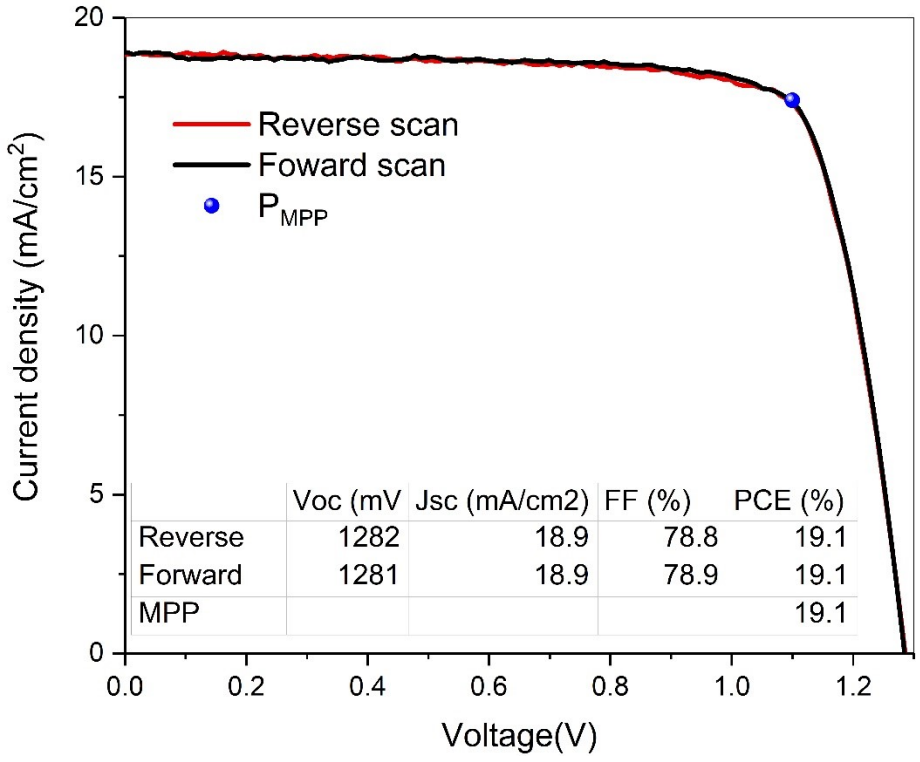


| | Voc (mV | Jsc (mA/cm2) | FF (%) | PCE (%) |
|---|---|---|---|---|
| Reverse | 1282 | 18.9 | 78.8 | 19.1 |
| Forward | 1281 | 18.9 | 78.9 | 19.1 |
| MPP | | | | 19.1 |

**Figure S2.** JV curves of the champion cell passivated with n-OABr.

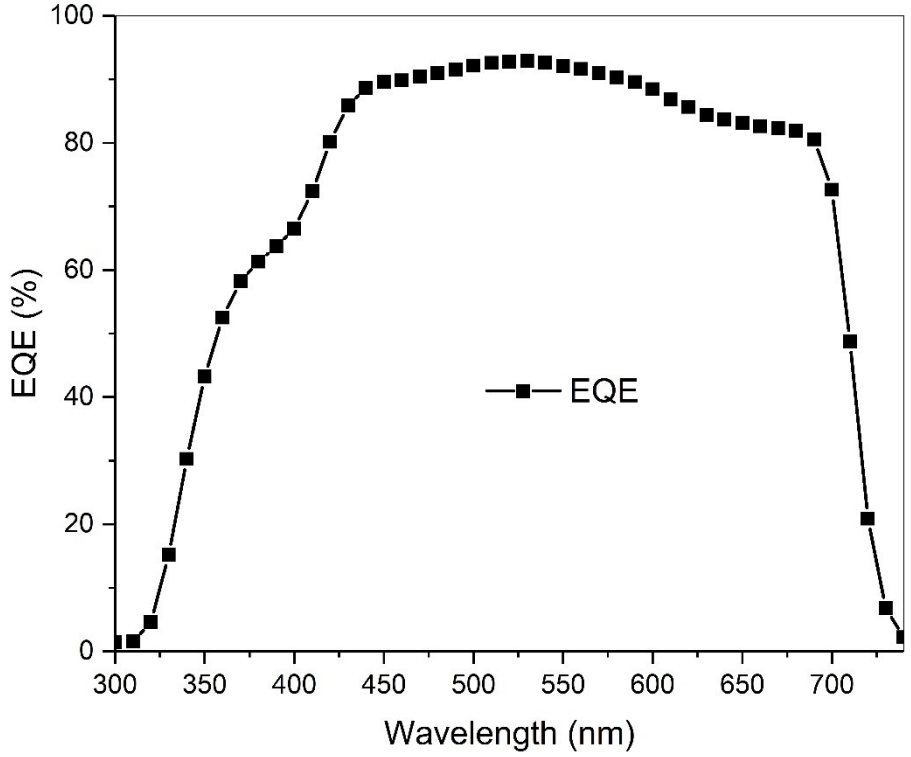


**Figure S3.** External Quantum Efficiency (EQE) of a perovskite solar cell passivated with n-OABr. The integrated $J_{SC}$ is 17.94 mA/cm$^2$, which is within $\pm$ 5% from the value extracted from the JV curves.

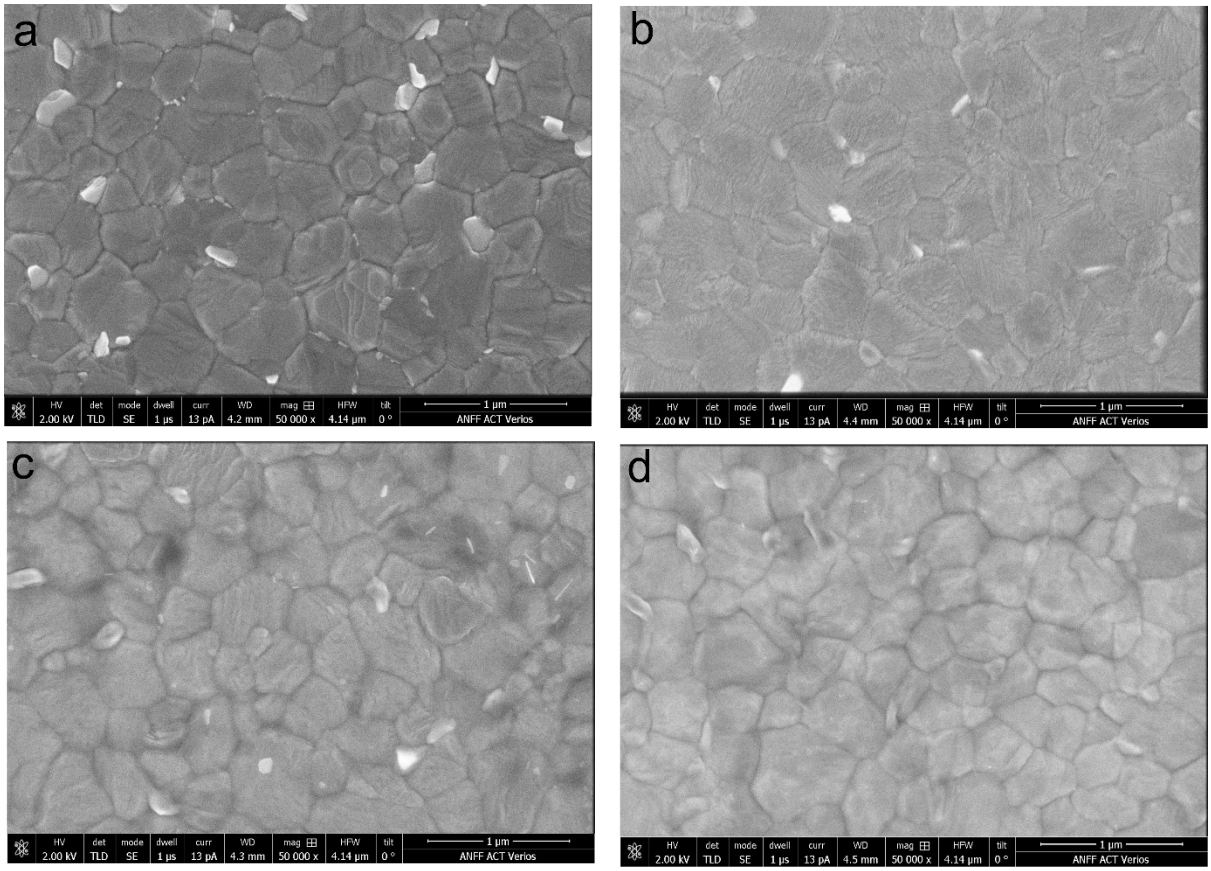


**Figure S4.** SEM images of **a** - control perovskite film, perovskite film passivated with **b** - n-BABr, **c** - n-OABr and **d** - n-DABr.

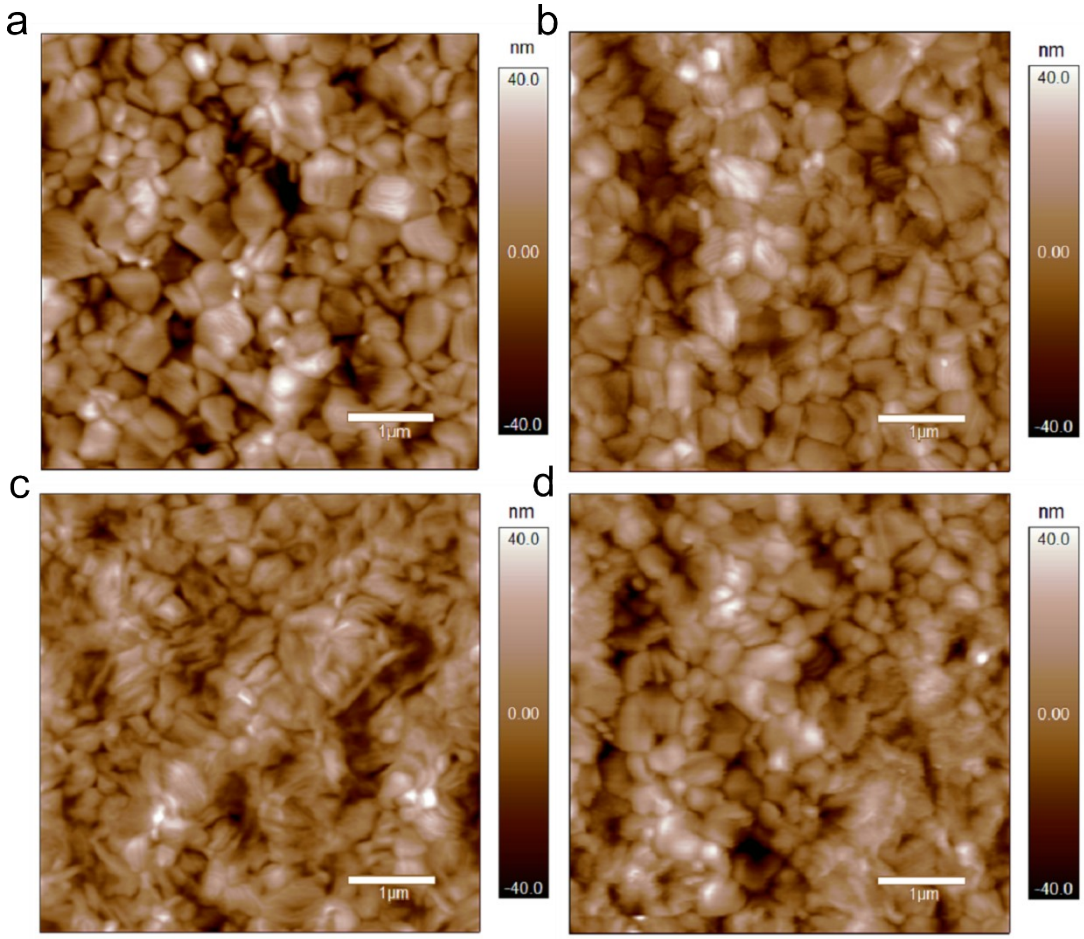


**Figure S5.** Atomic Force Miscroscopy images of perovskite films. **a** – control non-passivated film with surface roughness of 14.3 nm, **b** - n-BABr passivated film with surface roughness of 12.4 nm, **c** - n-OABr passivated film with surface roughness of 11.4 nm, **d** - n-DABr passivated film with surface roughness of 12.43 nm.

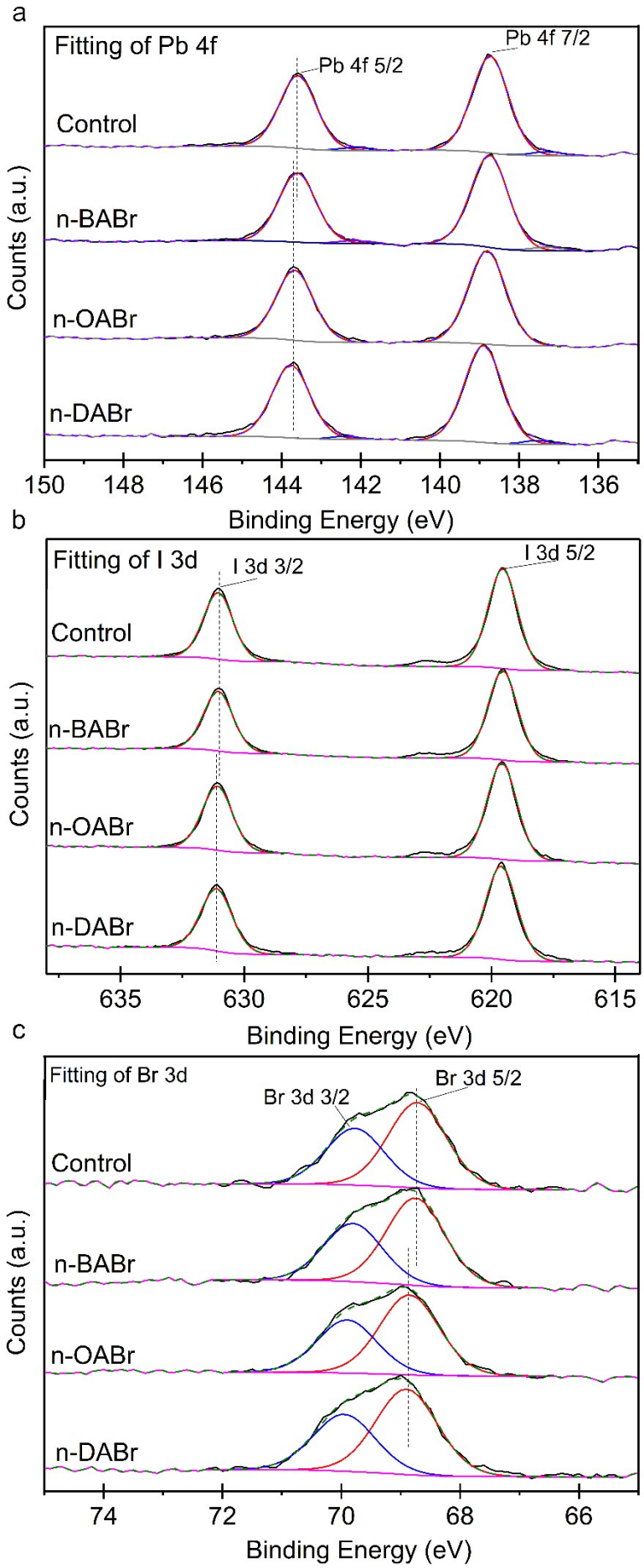
a
Fitting of Pb 4f
Pb 4f 5/2
Pb 4f 7/2
Control
n-BABr
n-OABr
n-DABr
Counts (a.u.)
150
148
146
144
142
140
138
136
Binding Energy (eV)
b
Fitting of I 3d
I 3d 3/2
I 3d 5/2
Control
n-BABr
n-OABr
n-DABr
Counts (a.u.)
635
630
625
620
615
Binding Energy (eV)
c
Fitting of Br 3d
Br 3d 3/2
Br 3d 5/2
Control
n-BABr
n-OABr
n-DABr
Counts (a.u.)
74
72
70
68
66
Binding Energy (eV)

**Figure S6.** Pb 4f, I 3d and Br 3d XPS spectra of control perovskite film and films passivated with different alkylammomium organic cations. The dash lines in each figure indicate the peak shift in the spectra of perovskite films pasivated with long chain length material (n-OABr and n-DABr) compared to the control sample and sample passivated with short chain length material (n-BABr).

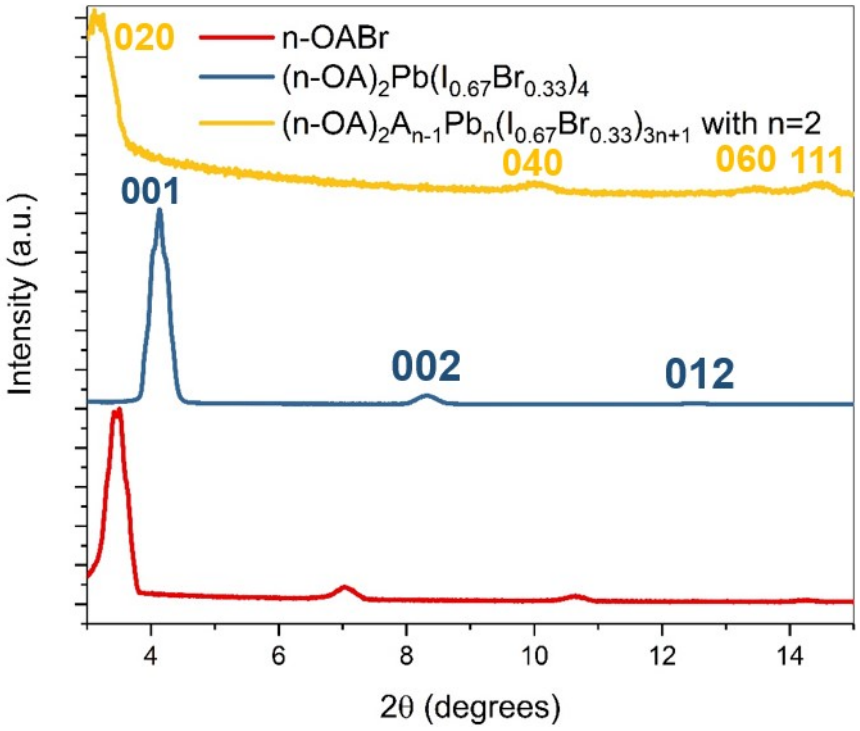


**Figure S7.** n-OABr (yellow, main peak at $2\theta = 3.49^{o}$), pure 2D perovskite phase (n-$OA)_2Pb(I_{0.67}Br_{0.33})_4$ (blue, main peak at $2\theta = 4.14^{o}$) and quasi-2D Ruddlesden Popper perovskite phase (n-$OA)_2A_{n-1}Pb_n(I_{0.67}Br_{0.33})_{3n+1}$ (red, $n = 2$ and A is the mixture of FA, MA, Cs and Rb, main peak at $2\theta = 3.12^{o}$)

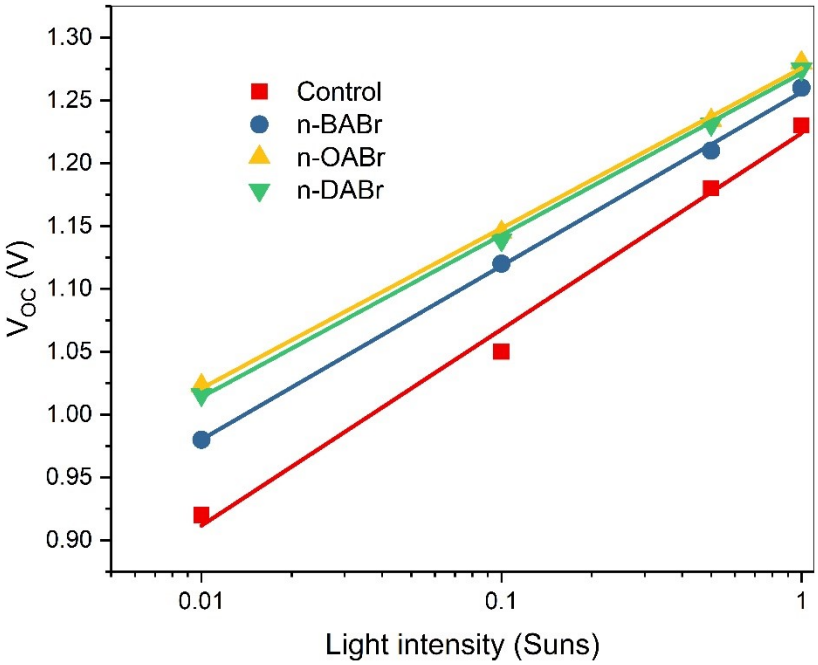


**Figure S8.** Light intensity – dependent VOC measurements of perovskite solar cells passivated with different organic cations. The measurements were performed when the device temperature was kept at 25 °C.

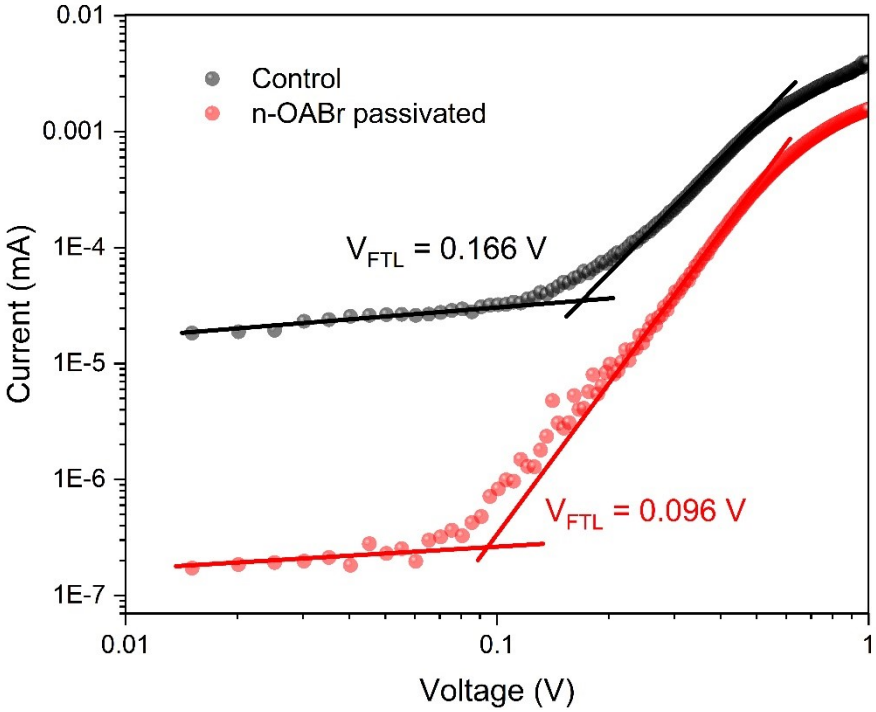


**Figure S9.** Space-charge-limit current measurements of hole-only devices with a structure glass/ITO/P3HT/perovskite/passivation layer/Spiro-MeOTAD/Au.

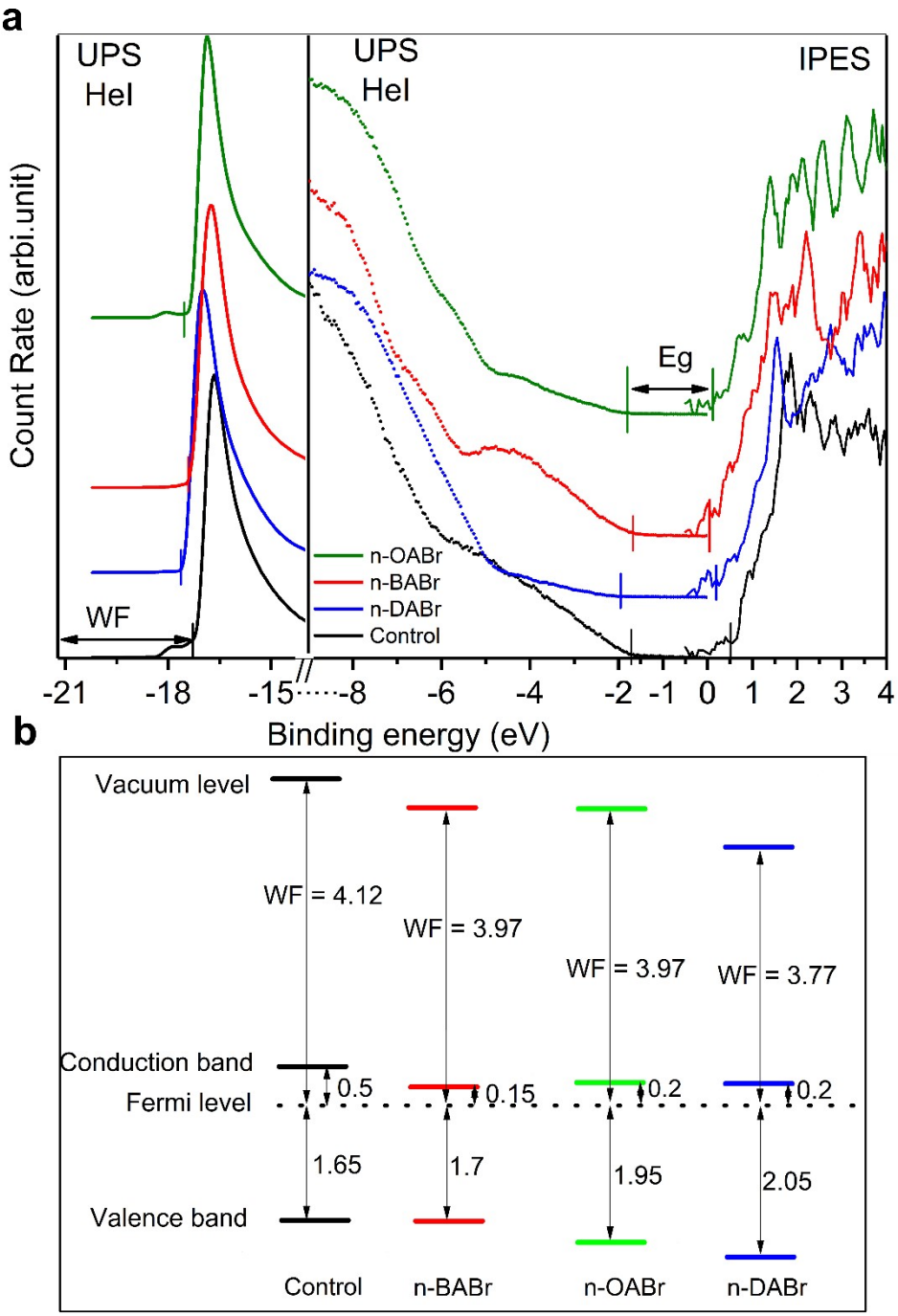


**Figure S10. a** - Ultraviolet photoelectron spectroscopy (UPS) and inverse photoemission spectroscopy (IPES) measurements of perovskite films with different passivations. **b** – Energy level diagram of perovskite films extracted from the ultraviolet photoelectron spectroscopy (UPS) and inverse photoemission spectroscopy (IPES) spectra. The uncertainty of the measured values is ±0.1 eV.

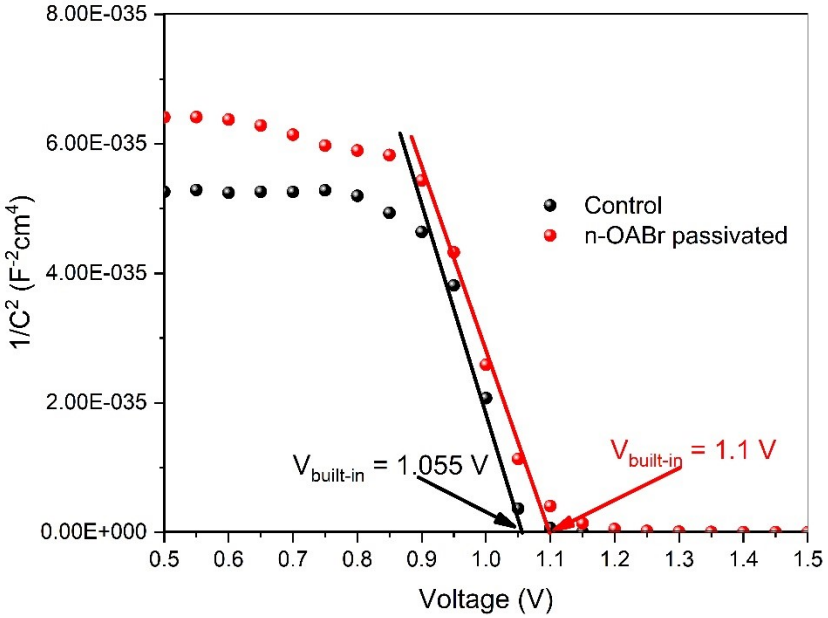


**Figure S11.** Capacitance-voltage measurements of a control perovskite cell and a device passivated with n-OABr.

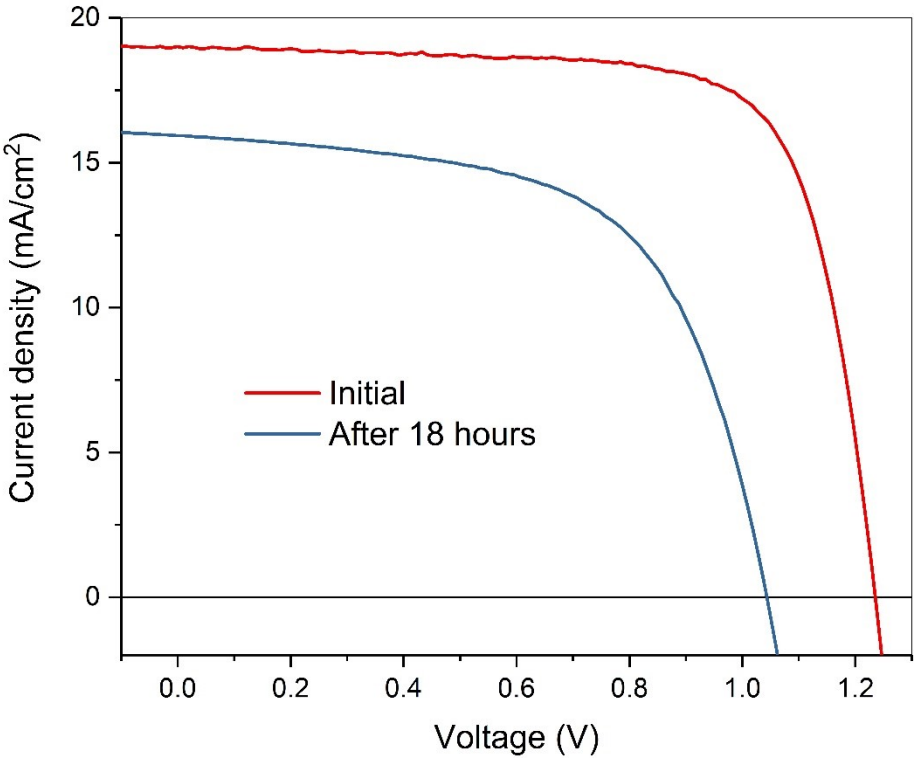


**Figure S12.** The moisture stability of control devices with Spiro-MeOTAD HTL details in a humid environment (RH between 70% to 85%) for 18 hours. The efficiency was degraded from 17.3% to 10.1% after 18 hours.

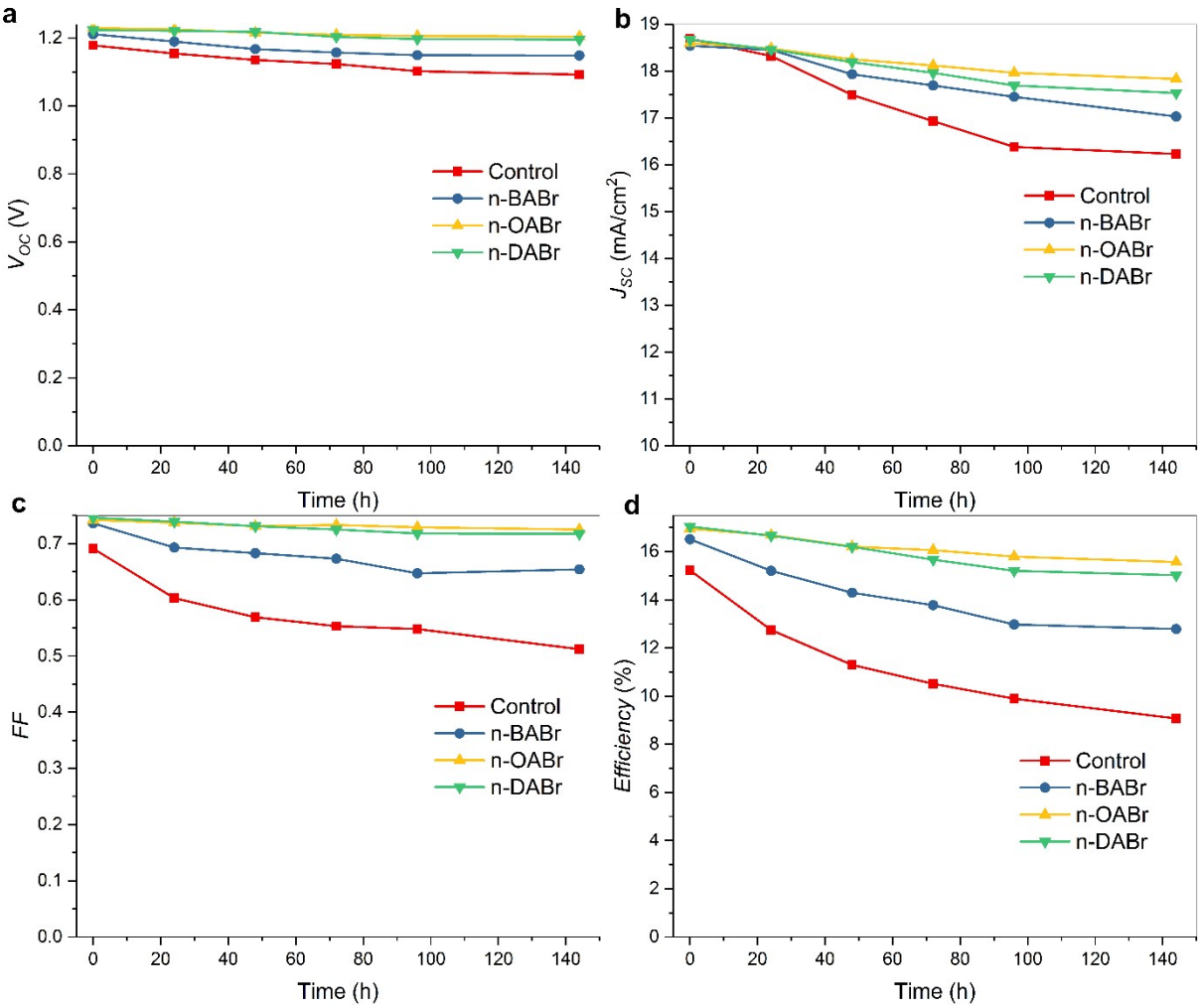


**Figure S13.** The details of all the photovoltaic parameters **a** - $V_{OC}$, **b** - $J_{SC}$, **c** - *FF* and **d** - *Efficiency*) of the devices during the moisture exposure.

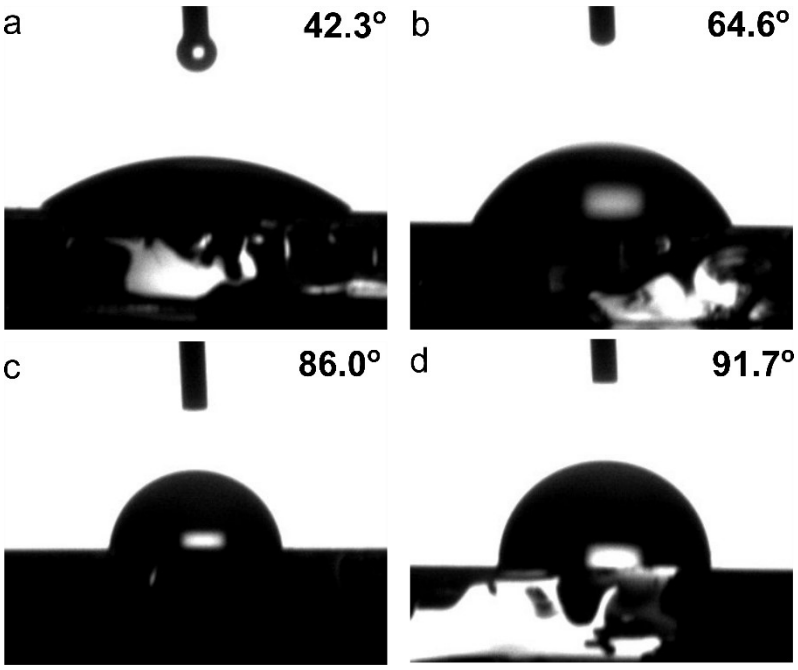

**Figure S14.** Contact angle measurements of perovskite films **a** - control perovskite film, perovskite film passivated with **b** - n-BABr, **c** - n-OABr and **d** - n-DABr.

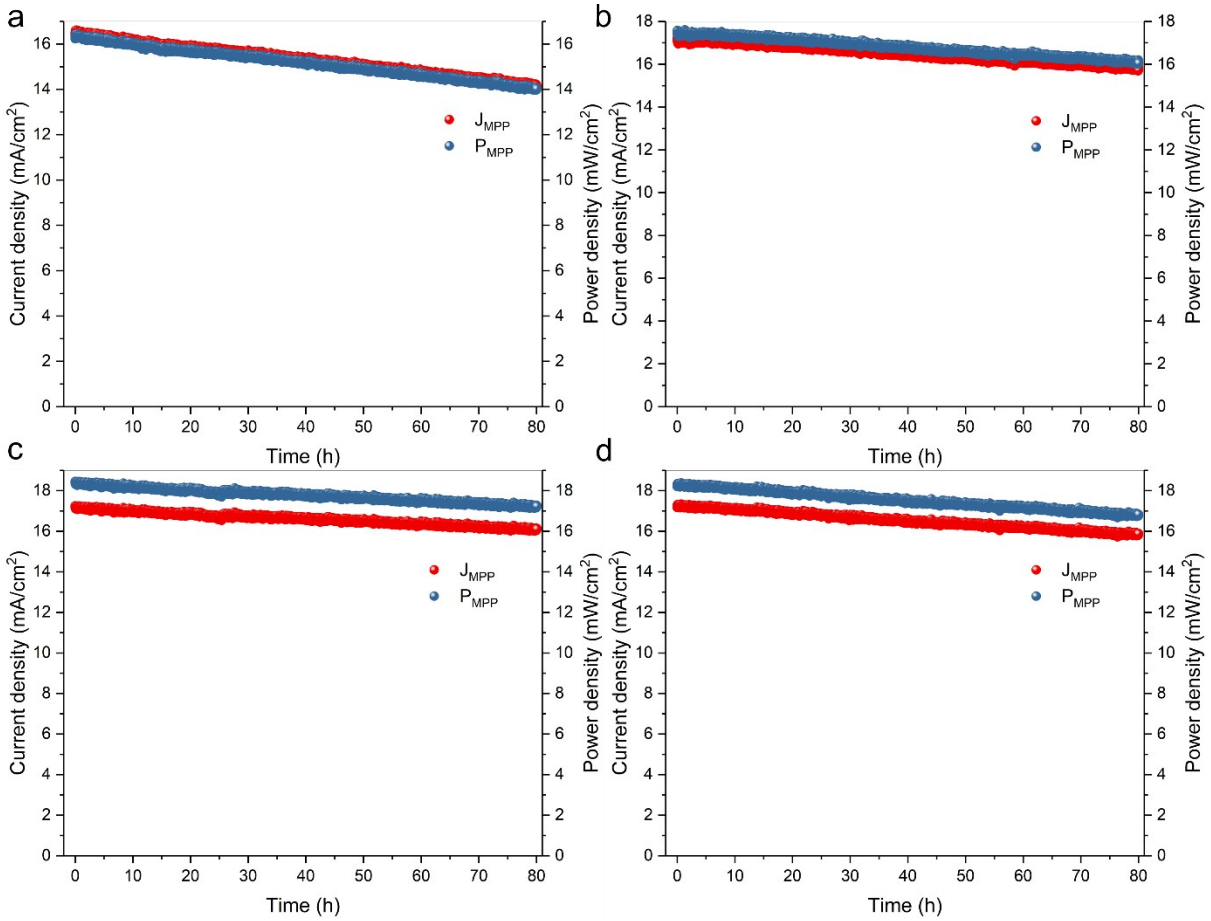


**Figure S15.** The details of light stability of perovskite solar cells with Sprio-MeOTAD HTL **a** – control device was monitored at a fixed voltage of 0.99 V, **b** – n-BABr passivated device was monitored at 1.02 V, **c** – n-OABr passivated device was monitored at 1.07 V and **d** – n-DABr passivated device was monitored at 1.06 V for 80 hours. All the devices were kept inside a nitrogen environment and the temperature was maintained at 25 $^{o}$C during the tests.

**Table S1.** Summary of photovoltaic parameters of perovskite solar cells passivating with different alkylammonium cations. More than 10 devices were fabricated in each condition.

| **Conditions** | **Scan direction** | **$V_{OC}$ (mV)** | **$J_{SC}$ (mA/cm$^2$)** | **FF (%)** | **Efficiency (%)** |
|---|---|---|---|---|---|
| **Control** | Forward | 1229 ± 10 | 18.8 ± 0.1 | 71.2 ± 1.9 | 16.5 ± 0.4 |
| | Reverse | 1235 ± 4 | 18.8 ± 0.1 | 72.9 ± 0.9 | 16.9 ± 0.4 |
| **n-BABr** | Forward | 1261 ± 3 | 18.8 ± 0.1 | 75.7 ± 0.9 | 17.9 ± 0.3 |
| | Reverse | 1262 ± 2 | 18.8 ± 0.2 | 75.5 ± 0.9 | 17.9 ± 0.3 |
| **n-OABr** | Forward | 1271 ± 4 | 18.8 ± 0.2 | 77.2 ± 0.8 | 18.4 ± 0.3 |
| | Reverse | 1272 ± 5 | 18.8 ± 0.2 | 77.2 ± 0.9 | 18.4 ± 0.3 |
| **n-DABr** | Forward | 1267 ± 3 | 18.8 ± 0.2 | 77.0 ± 0.7 | 18.4 ± 0.3 |
| | Reverse | 1268 ± 3.6 | 18.8 ± 0.2 | 76.9 ± 0.7 | 18.4 ± 0.3 |

**Table S2.** Summary of wide-bandgap (1.7-1.80 eV) single-junction perovskite solar cells with PCE >17% reported since 2018.

| **Year published** | **Perovskite compositions** | **$E_g$ (eV)** | **PCE (%)** | **References** |
|---|---|---|---|---|
| 2018 | $K_{0.1}(Cs_{0.06}FA_{0.79}MA_{0.15})_{0.9}Pb(I_{0.4}Br_{0.6})_3$ | 1.78 | 17.5 | [13] |
| 2018 | $FA_{0.83}Cs_{0.17}Pb(I_{0.6}Br_{0.4})_3$ | 1.75 | 17.8 | [14] |
| 2018 | $Cs_{0.17}FA_{0.83}PbI_{2.2}Br_{0.8}$ | 1.72 | 18.6 | [15] |
| 2018 | $Cs_{0.12}MA_{0.05}FA_{0.83}Pb(I_{0.6}Br_{0.4})_3$ | 1.75 | 19.1 | [16] |
| 2019 | $FA_{0.8}Cs_{0.2}Pb(I_{0.7}Br_{0.3})_3$ | 1.75 | 18.2 | [17] |
| 2019 | $Cs_{0.17}FA_{0.83}Pb(I_{0.6}Br_{0.4})_3$ | 1.72 | 19.8 | [18] |
| 2020 | $Rb_{0.05}(FA_{0.75}MA_{0.15}Cs_{0.1})_{0.95}PbI_2Br$ | 1.72 | 18.3 | [19] |
| 2020 | $FA_{0.8}Cs_{0.2}Pb(I_{0.7}Br_{0.3})_3$ | 1.73 | 18.8 | [20] |
| 2020 | $FA_{0.83}Cs_{0.17}Pb(I_{1-y}Br_y)_3$ | 1.74 | 17.2 | [21] |
| 2020 | $FA_{0.8}Cs_{0.2}Pb(I_{0.7}Br_{0.3})_3$ | 1.73 | 18.5 | [22] |
| 2020 | $Cs_{0.05}FA_{0.79}MA_{0.16}Pb(I_{0.6}Br_{0.4})_3$ | 1.75 | 18.4 | [23] |
| 2020 | $Cs_{0.15}FA_{0.85}Pb(I_{0.6}Br_{0.4})_3$ | 1.76 | 18.1 | [24] |
| 2021 | $(FA_{0.79}MA_{0.16}Cs_{0.05})_{0.95}Rb_{0.05}Pb(I_{0.6}Br_{0.4})_3$ | 1.78 | 17.7 | [25] |
| 2021 | $CH_3NH_3Pb(I_{0.8}Br_{0.2})_3$ | 1.72 | 18.9 | [26] |
| 2021 | $Rb_{0.05}(FA_{0.75}MA_{0.15}Cs_{0.1})_{0.95}PbI_2Br$ | 1.72 | 19.1 | This work |

**Table S3.** Pb Time of Flight onset, Pb Energy loss difference and the calculated thickness of the organic cation layer without Pb content.

| Sample | Pb TOF onset (µs) | Pb Energy loss difference (eV) | Thickness of the layer without Pb content (Å) |
|---|---|---|---|
| 3D control | 3.59 | 0 | 0 |
| n-OABr | 3.65 | 95 ± 10 | 16 ± 4 |

**Table S4.** Diode ideality factors of perovskite cells passivated with different organic cations calculated from the light intensity – dependent $V_{OC}$ measurements using the equation:

$$n_{id} = \frac{e \quad dV_{OC}}{k_B T \; d\ln \frac{I}{I_{1\,sun}}}.$$

| Sample | $n_{id}$ |
|---|---|
| Control | 1.38 |
| n-BABr | 1.22 |
| n-OABr | 1.13 |
| n-DABr | 1.14 |

**References**


[1] D. Walter, Y. Wu, T. Duong, J. Peng, L. Jiang, K.C. Fong, K. Weber, On the Use of Luminescence Intensity Images for Quantified Characterization of Perovskite Solar Cells: Spatial Distribution of Series Resistance, Adv. Energy Mater., 8 (2018) 1701522.

[2] T. Duong, Y. Wu, H. Shen, J. Peng, S. Zhao, N. Wu, M. Lockrey, T. White, K. Weber, K. Catchpole, Light and elevated temperature induced degradation (LeTID) in perovskite solar cells and development of stable semi-transparent cells, Sol. Energy Mater. Sol. Cells, 188 (2018) 27-36.

[3] K. Volgmann, F. Voigts, W. Maus-Friedrichs, The interaction of H2O molecules with iron films studied with MIES, UPS and XPS, Surface Science, 606 (2012) 858-864.

[4] S. Oswald, Growth studies of Ti-based films deposited on Si and SiO2 using angle-resolved XPS, Surface and Interface Analysis, 42 (2010) 1289-1294.

[5] F.M. Spirkl, S. Kunz, F.F. Schweinberger, A.N. Farnbacher, R. Schroter, U. Heiz, Improving metastable impact electron spectroscopy and ultraviolet photoelectron spectroscopy signals by means of a modified time-of-flight separation, Rev Sci Instrum, 83 (2012) 013114.

[6] K. Volgmann, F. Voigts, W. Maus-Friedrichs, The interaction of H2O molecules with iron films studied with MIES, UPS and XPS, Surface Science, 606 (2012) 858-864.

[7] S. Park, J. Jeong, G. Hyun, M. Kim, H. Lee, Y. Yi, The origin of high PCE in PTB7 based photovoltaics: proper charge neutrality level and free energy of charge separation at PTB7/PC71BM interface, Sci Rep, 6 (2016) 35262.

[8] G. Krishnan, H.S. Al Qahtani, J. Li, Y. Yin, N. Eom, V.B. Golovko, G.F. Metha, G.G. Andersson, Investigation of Ligand-Stabilized Gold Clusters on Defect-Rich Titania, The Journal of Physical Chemistry C, 121 (2017) 28007-28016.

[9] Y. Yin, D.A. Lewis, G.G. Andersson, Influence of Moisture on the Energy-Level Alignment at the MoO3/Organic Interfaces, ACS Appl Mater Interfaces, 10 (2018) 44163-44172.

[10] C.D.Wagner, Sensitivity factors for XPS analysis of surface atoms, Journal of Electron Spectroscopy and Related Phenomena, 32 (1983) 99-102.

[11] G. Andersson, H. Morgner, Investigations on solutions of tetrabutylonium salts in formamide with NICISS and ICISS: Concentration depth profiles and composition of the outermost layer, Surface Science - SURFACE SCI, 445 (2000) 89-99.

[12] A.R.M. Alharbi, J.M. Andersson, I. Köper, G.G. Andersson, Investigating the Structure of Self-Assembled Monolayers Related to Biological Cell Membranes, Langmuir, 35 (2019) 14213-14221.

[13] M. Abdi-Jalebi, Z. Andaji-Garmaroudi, S. Cacovich, C. Stavrakas, B. Philippe, J.M. Richter, M. Alsari, E.P. Booker, E.M. Hutter, A.J. Pearson, S. Lilliu, T.J. Savenije, H.

Rensmo, G. Divitini, C. Ducati, R.H. Friend, S.D. Stranks, Maximizing and stabilizing luminescence from halide perovskites with potassium passivation, Nature, 555 (2018) 497-501.

[14] J. Kim, M.I. Saidaminov, H. Tan, Y. Zhao, Y. Kim, J. Choi, J.W. Jo, J. Fan, R. Quintero-Bermudez, Z. Yang, L.N. Quan, M. Wei, O. Voznyy, E.H. Sargent, Amide-Catalyzed Phase-Selective Crystallization Reduces Defect Density in Wide-Bandgap Perovskites, Adv. Mater., 30 (2018) 1706275.

[15] Y. Zhou, Y.-H. Jia, H.-H. Fang, M.A. Loi, F.-Y. Xie, L. Gong, M.-C. Qin, X.-H. Lu, C.-P. Wong, N. Zhao, Composition-Tuned Wide Bandgap Perovskites: From Grain Engineering to Stability and Performance Improvement, Adv. Energy Mater., 28 (2018) 1803130.

[16] H. Tan, F. Che, M. Wei, Y. Zhao, M.I. Saidaminov, P. Todorović, D. Broberg, G. Walters, F. Tan, T. Zhuang, B. Sun, Z. Liang, H. Yuan, E. Fron, J. Kim, Z. Yang, O. Voznyy, M. Asta, E.H. Sargent, Dipolar cations confer defect tolerance in wide-bandgap metal halide perovskites, Nat. Commun., 9 (2018) 3100.

[17] C. Chen, Z. Song, C. Xiao, D. Zhao, N. Shrestha, C. Li, G. Yang, F. Yao, X. Zheng, R.J. Ellingson, C.-S. Jiang, M. Al-Jassim, K. Zhu, G. Fang, Y. Yan, Achieving a high open-circuit voltage in inverted wide-bandgap perovskite solar cells with a graded perovskite homojunction, Nano Energy, 61 (2019) 141-147.

[18] S. Gharibzadeh, B. Abdollahi Nejand, M. Jakoby, T. Abzieher, D. Hauschild, S. Moghadamzadeh, J.A. Schwenzer, P. Brenner, R. Schmager, A.A. Haghighirad, L. Weinhardt, U. Lemmer, B.S. Richards, I.A. Howard, U.W. Paetzold, Record Open-Circuit Voltage Wide-Bandgap Perovskite Solar Cells Utilizing 2D/3D Perovskite Heterostructure, Adv. Energy Mater., 9 (2019) 1803699.

[19] T. Duong, H. Pham, T.C. Kho, P. Phang, K.C. Fong, D. Yan, Y. Yin, J. Peng, M.A. Mahmud, S. Gharibzadeh, B.A. Nejand, I.M. Hossain, M.R. Khan, N. Mozaffari, Y. Wu, H.

Shen, J. Zheng, H. Mai, W. Liang, C. Samundsett, M. Stocks, K. McIntosh, G.G. Andersson, U. Lemmer, B.S. Richards, U.W. Paetzold, A. Ho-Ballie, Y. Liu, D. Macdonald, A. Blakers, J. Wong-Leung, T. White, K. Weber, K. Catchpole, High Efficiency Perovskite-Silicon Tandem Solar Cells: Effect of Surface Coating versus Bulk Incorporation of 2D Perovskite, Adv. Energy Mater., 10 (2020) 1903553.

[20] C. Chen, Z. Song, C. Xiao, R.A. Awni, C. Yao, N. Shrestha, C. Li, S.S. Bista, Y. Zhang, L. Chen, R.J. Ellingson, C.-S. Jiang, M. Al-Jassim, G. Fang, Y. Yan, Arylammonium-Assisted Reduction of the Open-Circuit Voltage Deficit in Wide-Bandgap Perovskite Solar Cells: The Role of Suppressed Ion Migration, ACS Energy Lett., 5 (2020) 2560-2568.

[21] S. Gharibzadeh, I.M. Hossain, P. Fassl, B.A. Nejand, T. Abzieher, M. Schultes, E. Ahlswede, P. Jackson, M. Powalla, S. Schäfer, M. Rienäcker, T. Wietler, R. Peibst, U. Lemmer, B.S. Richards, U.W. Paetzold, 2D/3D Heterostructure for Semitransparent Perovskite Solar Cells with Engineered Bandgap Enables Efficiencies Exceeding 25% in Four-Terminal Tandems with Silicon and CIGS, Adv. Funtional Mater., 30 (2020) 1909919.

[22] T. Bu, J. Li, Q. Lin, D.P. McMeekin, J. Sun, M. Wang, W. Chen, X. Wen, W. Mao, C.R. McNeill, W. Huang, X.-L. Zhang, J. Zhong, Y.-B. Cheng, U. Bach, F. Huang, Structure engineering of hierarchical layered perovskite interface for efficient and stable wide bandgap photovoltaics, Nano Energy, 75 (2020) 104917.

[23] L. Wang, G. Wang, Z. Yan, J. Qiu, C. Jia, W. Zhang, C. Zhen, C. Xu, K. Tai, X. Jiang, S. Yang, Potassium-Induced Phase Stability Enables Stable and Efficient Wide-Bandgap Perovskite Solar Cells, Solar RRL, 4 (2020) 2000098.

[24] Y. Chen, W. Tang, Y. Wu, R. Yuan, J. Yang, W. Shan, S. Zhang, W.-H. Zhang, Multilayer Cascade Charge Transport Layer for High-Performance Inverted Mesoscopic All-Inorganic and Hybrid Wide-Bandgap Perovskite Solar Cells, Solar RRL, 4 (2020) 2000344.

[25] K.M. Reza, A. Gurung, B. Bahrami, A.H. Chowdhury, N. Ghimire, R. Pathak, S.I. Rahman, M.A.R. Laskar, K. Chen, R.S. Bobba, B.S. Lamsal, L.K. Biswas, Y. Zhou, B. Logue, Q. Qiao, Grain Boundary Defect Passivation in Quadruple Cation Wide-Bandgap Perovskite Solar Cells, Solar RRL, 5 (2021) 2000740.

[26] Z. Liu, J. Siekmann, B. Klingebiel, U. Rau, T. Kirchartz, Interface Optimization via Fullerene Blends Enables Open-Circuit Voltages of 1.35 V in CH3NH3Pb(I0.8Br0.2)3 Solar Cells, Adv. Energy Mater., 11 (2021) 2003386.